Progress In Electromagnetics Research C, Vol. 170, 151–161, 2026

PIER C

(Received 24 March 2026, Accepted 26 April 2026, Scheduled 11 May 2026)

A Novel Key-Shaped Miniaturized High-Isolation MIMO Antenna for UWB Applications

Xinyu Liu[1], Han Lin[1, *], and Zhonggen Wang[1, 2]

[1] *School of Electrical and Information Engineering, Anhui University of Science and Technology, Huainan, Anhui, 232001, China*
[2] *Key Laboratory of Intelligent Computing and Signal Processing, Ministry of Education, Hefei, Anhui, 230039, China*

ABSTRACT: This paper presents a novel key-shaped miniaturized four-port MIMO antenna designed for ultra-wideband (UWB) applications. The proposed antenna consists of four orthogonally and symmetrically arranged key-shaped radiating elements. By integrating semi-circular patches at the edges of rectangular radiators, multiple resonance modes are excited to significantly broaden the impedance bandwidth and optimize matching. To suppress mutual coupling within a compact footprint, an enhanced cross-shaped defected ground structure (DGS) is implemented, which effectively blocks surface wave propagation by utilizing narrow rectangular stubs. Experimental results demonstrate that the antenna achieves a continuous impedance bandwidth from 4.4 to 26 GHz, corresponding to a fractional bandwidth of 141.5%. Throughout the operating band, the port isolation remains better than 28 dB, while the envelope correlation coefficient (ECC) is lower than 0.00013, ensuring excellent diversity performance. Furthermore, the antenna, fabricated on an FR4 substrate with a compact size of $47 \times 47 \times 1.6\,\text{mm}^3$, maintains a radiation efficiency between 67.4% and 92.6%. With its superior bandwidth, high isolation, and exceptionally low correlation, the proposed design offers a robust solution for high-performance UWB communication systems.

1. INTRODUCTION

Ultra-wideband (UWB) technology has emerged as a pivotal paradigm in modern wireless communications, distinguished by its high-speed data transmission and robust link reliability [1]. Despite its transformative potential, the practical deployment of UWB is often constrained by its low power spectral density and inherent vulnerability to severe multipath fading, which typically limits its operation to short-range applications [2]. To overcome these channel impairments, the integration of Multiple-Input Multiple-Output (MIMO) technology with UWB systems has become an essential research frontier. This synergy not only mitigates multipath effects but also significantly enhances channel capacity and spectral efficiency. Consequently, the development of UWB-MIMO antennas has gained considerable momentum, necessitating designs that concurrently satisfy requirements for compact footprints, broad operational bandwidths, and stable radiation characteristics [3–5].

A primary challenge in the realization of high-performance UWB-MIMO systems is the suppression of mutual coupling between closely spaced radiating elements [6, 7]. In compact MIMO arrays, strong electromagnetic interaction can severely degrade radiation efficiency and compromise the envelope correlation coefficient (ECC) [8]. While various decoupling strategies — such as neutralization lines, parasitic meandered structures, and metallic reflectors — have been reported in the literature, achieving high isolation (> 25 dB) across the entire UWB spectrum remains a formidable hurdle [9]. This is particularly evident in designs utilizing a common ground plane, where correlated surface currents facilitate strong inter-element coupling [10, 11]. Although slot antennas are frequently preferred for their favorable impedance bandwidth and ease of integration, maintaining wideband decoupling within a shared-ground architecture persists as a critical design bottleneck [12].

To address these limitations, this study proposes a novel, compact four-port UWB-MIMO antenna architecture. The design is based on a connected-ground slot configuration excited by optimized L-shaped stub feedlines, which serve to enhance impedance matching and facilitate high isolation across the desired frequency range. By strategically engineering the feed geometry and slot dimensions, the proposed antenna achieves superior diversity performance and broadband characteristics. Furthermore, this study provides an in-depth exploration of the experimental methodology and practical challenges associated with the characterization of four-port compact MIMO systems. The proposed design offers a robust solution for high-speed, short-range wireless applications, where both miniaturization and high isolation are paramount.

2. ANTENNA DESIGN PROCESS

2.1. Antenna Geometry

The UWB MIMO antenna proposed in this study is fabricated on a low-cost FR4 dielectric substrate (a relative permittivity of 4.4, and a loss tangent of 0.02) with a compact overall footprint of $47 \times 47 \times 1.6\,\text{mm}^3$. Regarding the top-layer structure, the MIMO system consists of four antenna elements arranged in an orthogonal and symmetrical configuration. This layout is specifically designed to suppress mutual coupling between elements by leveraging spatial and polarization diversity.

---

* Corresponding author: Han Lin (hanlin@aust.edu.cn).

doi:10.2528/PIERC26032404

Published by THE ELECTROMAGNETIC ACADEMY

TABLE 1. Optimized dimension of antenna parameters.

Parameter	L	L_1	L_2	L_3	L_4	L_5	L_6	L_7	L_8
Size (mm)	47	15.2	7	3.5	22	0.37	3	6.5	9
Parameter	L_9	W	W_1	W_2	W_3	W_4	W_5	W_6	W_7
Size (mm)	6.4	47	2	0.5	7.25	5	15	14	3.8
Parameter	R_1	R_2	R_3	R_4	R_5	R_6	R_7		
Size (mm)	1.5	3	1.5	3	2	3.5	0.75		

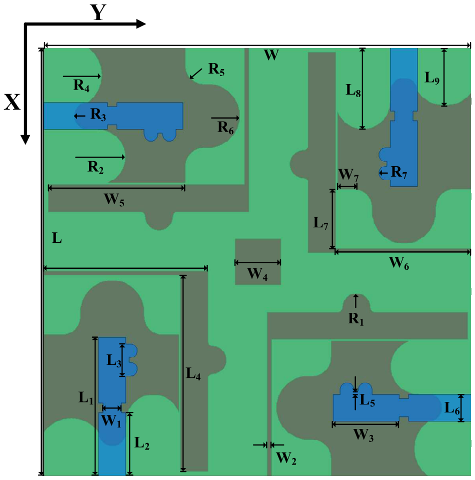

FIGURE 1. Structure and dimensions of the antenna.

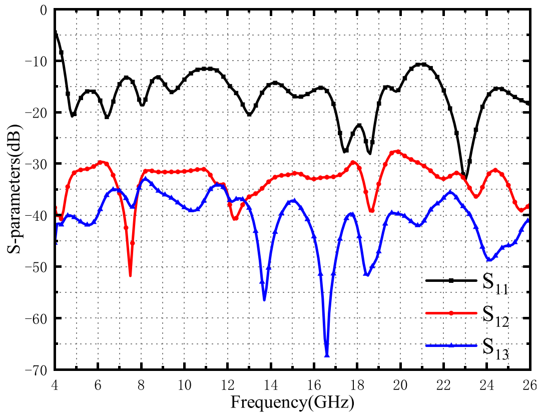

FIGURE 2. The S-parameters of the proposed antenna.

The radiating elements feature a unique "key-shaped" topology, which is a composite of a rectangular main patch and edge-loaded semi-circular stubs. This non-uniform geometric design aims to excite multiple resonance modes to broaden the impedance bandwidth, while the circular edges facilitate a smooth impedance transition. To ensure optimal impedance matching, the antenna is fed by a 50 Ω microstrip line featuring an integrated L-shaped matching stub. As depicted in Fig. 1, this stub is monolithically etched as a contiguous part of the feedline on the same copper layer, rather than being a discrete surface-mounted component. This integrated design functions as a parasitic tuning element to broaden the impedance bandwidth while maintaining a compact footprint and simplifying fabrication. For the bottom layer, a finely tuned Defected Ground Structure (DGS) is implemented, incorporating circular arc subtractions. This filleting technique optimizes surface current paths and minimizes parasitic reactance at high frequencies, thereby significantly enhancing the return loss characteristics across the entire UWB spectrum. To further improve isolation, the four independent ground branches are interconnected via narrow rectangular stubs to a central cross-shaped decoupling element. In addition to serving as a common reference ground, this structure introduces specific equivalent inductive/capacitive characteristics that act as a current-blocking mechanism. Consequently, surface wave propagation is effectively suppressed, ensuring superior decoupling performance for the high-integration MIMO system. The detailed geometric parameters of the antenna were optimized using electromagnetic simulation software, and the finalized dimensions are summarized in Table 1.

The simulated S-parameters of the proposed antenna are illustrated in Fig. 2. The results indicate that the antenna maintains continuous and stable impedance matching characteristics across the broad frequency range of 4.4–26 GHz. Moreover, the mutual coupling between the elements remains significantly low, with the port isolation exceeding 28 dB throughout the entire operating band. Such outstanding decoupling performance ensures the reliability of the MIMO system for high-speed data transmission.

2.2. Proposed Single Antenna Evolution

Figure 3 illustrates the structural evolution of the proposed UWB MIMO antenna and its corresponding S_{11} parameters. The initial design (Ant. 1) consists of four orthogonally arranged elements, each comprising a simple rectangular radiating patch, a microstrip feed line, and a rectangular ground plane. As depicted in the figure, the effective impedance bandwidth of Ant. 1 only covers two discrete bands: 5.60–8.26 GHz and 16.35–22.46 GHz. The significant frequency gap between these bands fails to meet the requirements for continuous UWB communication. To extend the bandwidth, multiple rectangular slots and stubs are integrated into the ground plane to form Ant. 2. This modification alters the surface current distribution, successfully exciting a new resonance mode within the 8.45–11.86 GHz range, which effectively fills the lower-frequency gap. However, the abrupt geometric transitions in the ground plane introduce impedance discontinuities, leading to a noticeable impedance mismatch at higher frequencies. To mitigate the high-frequency mismatch observed in Ant. 2, a rounding

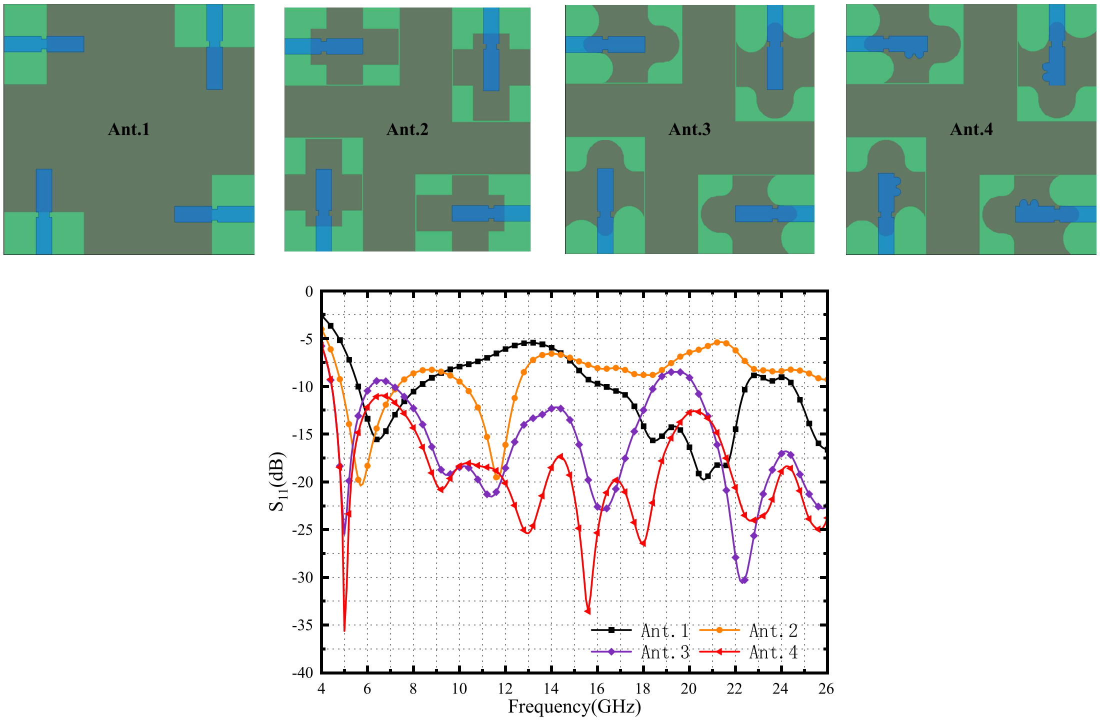

FIGURE 3. Evolution of antennas and corresponding S_{11} parameters.

technique is applied to the ground plane of Ant. 3. By replacing the rectangular sharp edges with smooth circular transitions, the parasitic reactance during electromagnetic wave transmission is minimized, thereby optimizing the high-frequency impedance matching. This improvement significantly reduces reflection loss across the upper-frequency range and further broadens the operating bandwidth. In the final configuration, two symmetrical semi-circular patches are added to the edges of the radiating patch for fine-tuning the input impedance. This refinement further enhances the stability of the overall impedance matching. Experimental results indicate that the finalized Ant. 4 achieves an $S_{11} < -10$ dB across an ultra-wide frequency range from 4.4 to 26 GHz, yielding a fractional bandwidth of 141.5%. This performance fully satisfies the stringent requirements for high-performance UWB systems.

2.3. Decoupling Design of the MIMO Antenna

Figure 4 illustrates the structural comparison and the corresponding S-parameters of the MIMO antenna before and after the integration of the isolation structure. Specifically, MIMO_1 corresponds to the aforementioned Ant. 4. Without an additional decoupling structure, the system already exhibits a degree of diversity performance, attributed to the orthogonal spatial orientation and sufficient physical separation between the antenna elements. However, the S-parameter curves reveal that the mutual coupling between diagonal elements S_{13} exceeds -20 dB in the high-frequency range of 15.77–23.07 GHz. This indicates significant electromagnetic interference between diagonal ports, which constrains the overall capacity and transmission reliability of the MIMO system.

To eliminate this high-frequency interference and comprehensively enhance isolation across the entire band, an improved cross-shaped decoupling structure is introduced based on the MIMO_1 configuration. This structure is electrically connected to the individual ground planes via narrow rectangular stubs, forming a functional common reference ground. This design not only provides a unified potential reference but, more importantly, also leverages the specific geometric distribution of the stubs and the cross-shaped structure to generate band-stop characteristics at mid-to-high frequencies. Consequently, the propagation of surface wave currents through the ground plane is effectively blocked.

Although the near-field coupling between the decoupling elements and the radiating patches excites additional resonance modes — resulting in more resonance dips in the S_{11} curve — the effective operating bandwidth remains stable within 4.4–26 GHz, maintaining its UWB performance. The most prominent improvement is observed in the decoupling of diagonal elements: the S_{13} of MIMO_2 is drastically suppressed, with mutual coupling levels dropping below -30 dB across the entire operating band. This improvement effectively eliminates the previously identified interference zones, demonstrating the superior efficacy of the proposed decoupling structure in suppressing mutual coupling and significantly enhancing the anti-interference capability of the MIMO antenna in complex electromagnetic environments.

2.4. Equivalent Circuit Analysis

To thoroughly reveal the electromagnetic characteristics of the proposed four-port MIMO antenna, Fig. 5 presents its equivalent lumped-element circuit model. In this model, the input

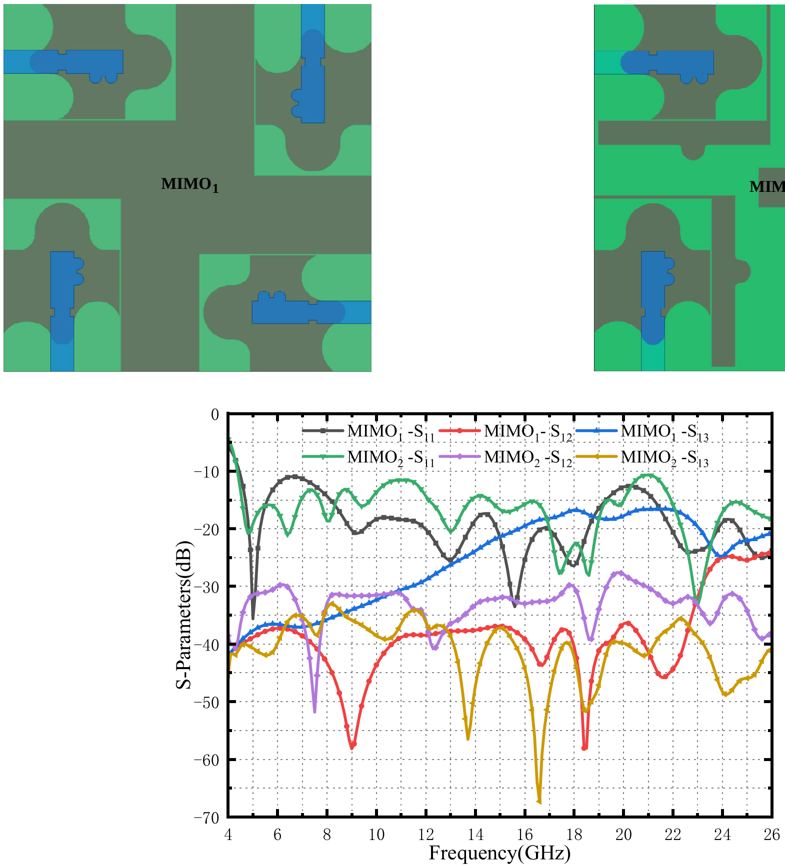

FIGURE 4. S-parameter diagrams of MIMO$_1$ and MIMO$_2$.

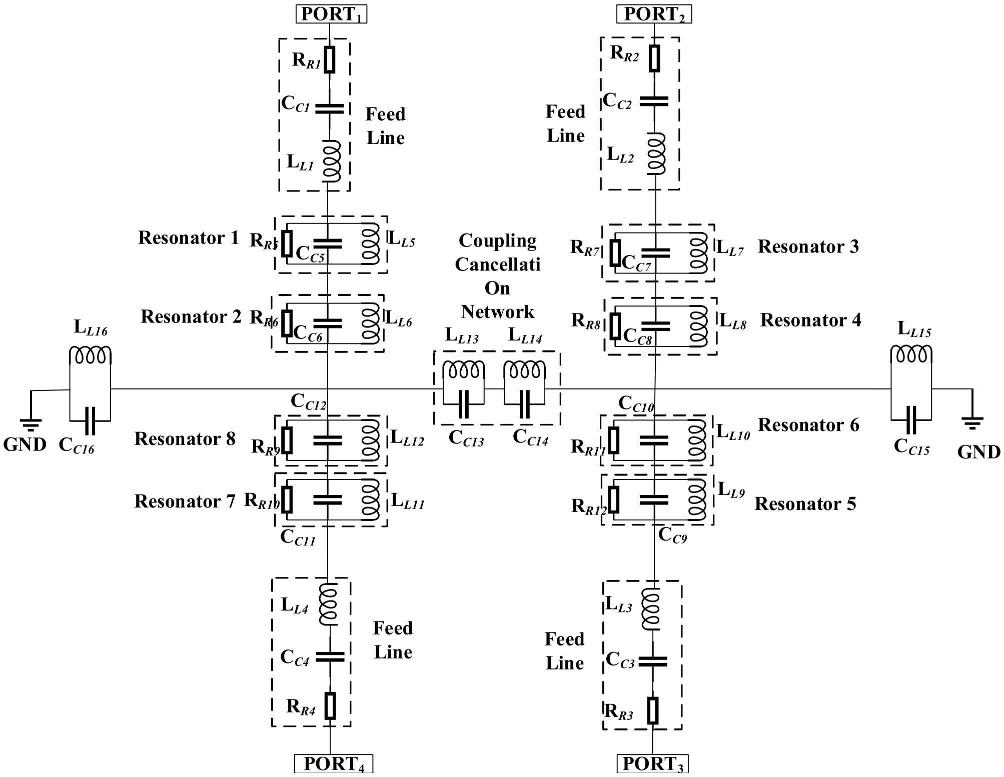

FIGURE 5. Equivalent circuit diagram.

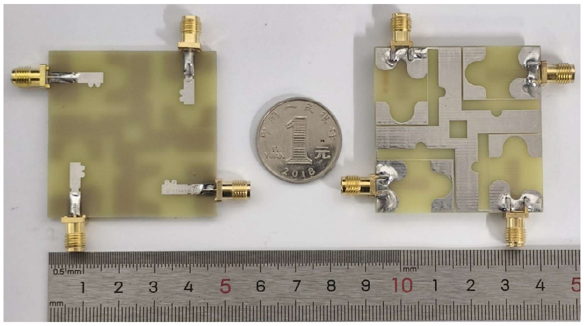

FIGURE 6. Photograph of the fabricated physical antenna.

section of each port (Port 1 to Port 4) incorporates a series LC matching network labeled "feed line", which effectively characterizes the impedance transformation between the 50 Ω microstrip feed line and the integrated L-shaped stub. The wideband radiation performance and multi-resonance behavior of the antenna elements are represented by multiple cascaded parallel LC resonators (Resonators 1–8), where each resonant loop corresponds to a specific frequency dip in the reflection coefficient S_{11} within the operating band of 4.4–26 GHz. Furthermore, a structure named the "coupling cancellation network" in the middle of the circuit connects the symmetric antenna branches to emulate the decoupling effect of the grounded configuration. This network introduces a compensatory coupling path to counteract mutual interference, thereby ensuring high isolation between ports. Finally, parasitic reactance elements connected to the ground points reflect the inherent capacitive and inductive properties of the structure, which collectively provide a comprehensive circuit-level theoretical basis for the high-speed communication performance and stable total all-directional radiation coefficient exhibited by the antenna.

3. ANTENNA PERFORMANCE ANALYSIS

3.1. Simulated and Measured S-Parameters

Following the electromagnetic simulation and optimization, the proposed UWB MIMO antenna was fabricated and experimentally validated, with the prototype displayed in Fig. 6 and the comparison between simulated and measured S-parameters, obtained via a Vector Network Analyzer (VNA), presented in Fig. 7. As observed from the results, the measured S_{11} curve maintains a high degree of consistency with the simulated trend across the entire operating bandwidth; although the number of measured resonance points is slightly reduced compared to the simulation — primarily due to fabrication tolerances, SMA connector soldering effects, and minor fluctuations in dielectric substrate parameters — the impedance bandwidth $S_{11} < -10\,\text{dB}$ still fully covers the 4.4–26 GHz range, effectively verifying the antenna's excellent impedance matching characteristics. Simultaneously, the measured isolation parameters (S_{12} and S_{13}) exhibit favorable agreement with the simulated data, remaining above 28 dB throughout the frequency band. This provides strong evidence that the modified cross-shaped ground decoupling structure possesses remarkable robustness, effectively counteracting the impact of practical fabrication errors and ensuring superior electromagnetic isolation between elements, with the overall measured performance aligning closely with the design expectations for high-performance UWB MIMO communication systems.

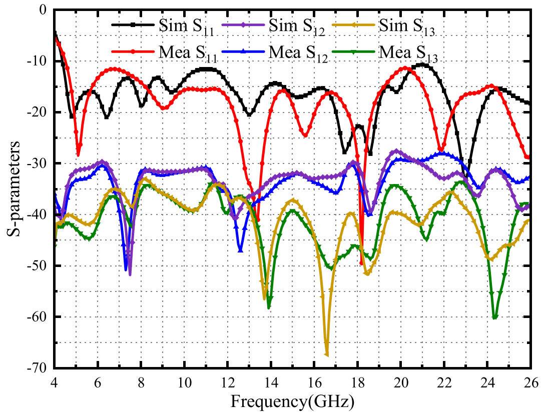

FIGURE 7. Comparison of simulated and measured S-parameters.

3.2. Antenna Current Analysis

The surface current distribution serves as a vital tool for elucidating the electromagnetic operating mechanism and the decoupling effectiveness of an antenna at specific resonant frequencies. As illustrated in Fig. 8, when Port 1 is excited and the remaining ports are terminated with 50 Ω matched loads, the intense current is primarily concentrated on the radiating element and the feedline of Port 1 at the four resonant frequencies (4.8 GHz, 9.6 GHz, 15.5 GHz, and 22.3 GHz), while the current flowing toward Ports 2, 3, and 4 is negligible, visually confirming the antenna's superior isolation. At the lower frequencies of 4.8 GHz and 9.6 GHz (Figs. 8(a)–(b)), the large physical spacing between elements relative to the wavelength, combined with the electrical isolation provided by the cross-shaped ground structure, prevents all but a minimal amount of current from diffusing across the isolation zone to adjacent ports; this is in perfect agreement with the extremely low S_{12} and S_{13} parameters observed in the low-frequency band. As the frequency increases to 15.5 GHz (Fig. 8(c)), despite the intensified near-field coupling caused by the increased electrical size of the radiating elements, the narrow rectangular stubs of the modified cross-structure effectively induce counter-currents, trapping most surface waves at the edges of the isolation structure and preventing current penetration into the non-excited elements. Even at the upper frequency of 22.3 GHz (Fig. 8(d)), where the significantly shortened wavelength increases the risk of mutual coupling, the cross-shaped decoupling structure still demonstrates remarkable energy confinement, minimizing high-frequency coupling currents and fully validating the effectiveness of the structure in enhancing isolation across the UWB range of 4.4–26 GHz.

3.3. Envelope Correlation Coefficient and Diversity Gain

In the design and evaluation of MIMO antenna systems, Envelope Correlation Coefficient (ECC) serves as a pivotal metric for assessing diversity performance, fundamentally quantifying

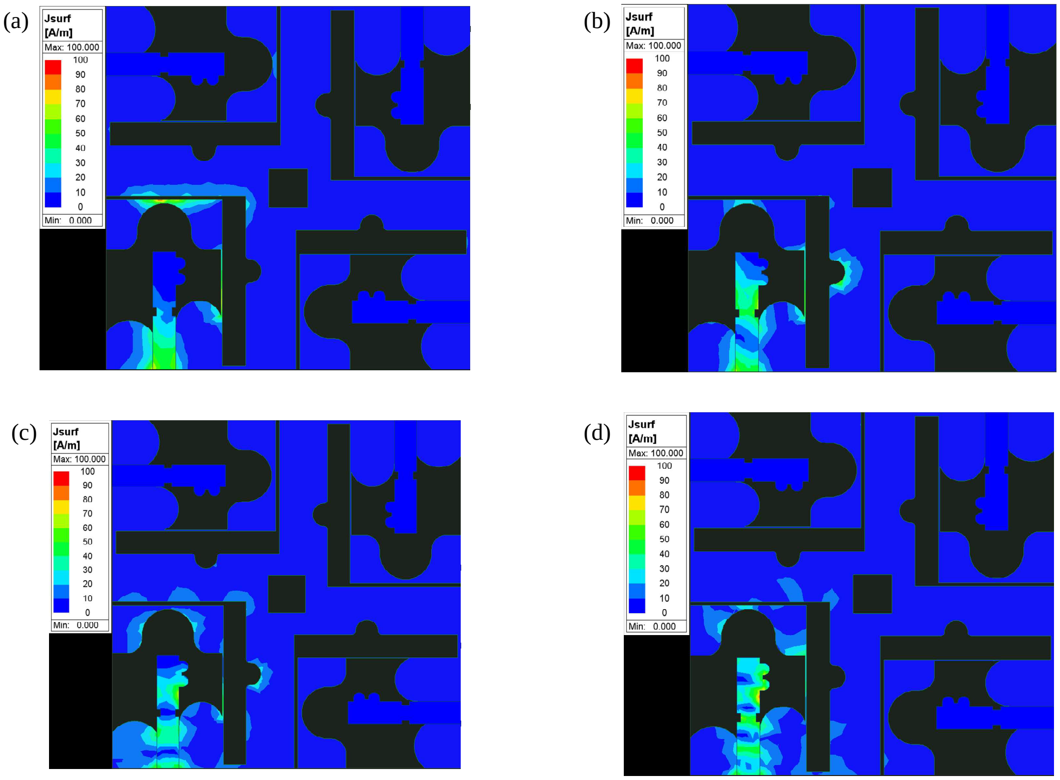

FIGURE 8. Current distribution diagram. (a) 4.8 GHz, (b) 9.6 GHz, (c) 15.5 GHz, (d) 22.3 GHz.

the statistical correlation between signals captured by individual radiating elements in complex multipath environments. Its value intuitively reflects the waveform overlap between different antenna branches, with a threshold of ECC < 0.5 generally adopted in both academia and industry as the criterion for ensuring sufficient statistical independence. In the limit where the ECC approaches zero, the amplitude and frequency characteristics of the signals across various branches behave as mutually uncorrelated random processes, implying that even if a specific branch experiences deep fading due to multipath effects, the remaining independent branches can still maintain high-quality signal transmission. Such a highly decoupled physical state not only endows the system with superior resistance to multipath fading and significantly enhanced diversity gain but also fully exploits the spatial multiplexing potential of the MIMO architecture by minimizing inter-element interference. Consequently, this leads to substantial improvements in spectral efficiency and system throughput while guaranteeing link robustness and an extremely low bit error rate (BER) for high-speed data transmission. The ECC can be expressed as follows:

$$\mathrm{ECC} = \frac{|S_{ii} * S_{ij} + S_{ji} * S_{jj}|^2}{\left(1 - |S_{ii}|^2 - S_{ij}^2\right)\left(1 - |S_{ji}|^2 - S_{jj}^2\right)} \tag{1}$$

Diversity gain (DG) serves as a critical figure of merit for assessing the enhancement of communication link reliability through spatial diversity techniques. Its primary significance lies in the combination of signals from multiple independent fading channels, which allows the receiver to achieve a more stabilized Signal-to-Noise Ratio (SNR) and significantly suppress fluctuations in signal intensity. The realization of diversity gain is profoundly dependent on complex multipath propagation environments; under such conditions, the signals captured by individual antenna elements exhibit uncorrelated fading characteristics, providing the physical prerequisite for diversity techniques to exploit spatial advantages. Without the support of a rich multipath environment, the improvement of diversity gain would be inherently constrained by physical limits. Therefore, a high level of diversity gain is not only a direct manifestation of enhanced signal stability but also a profound demonstration of the MIMO system's superior capability to mitigate multipath fading within the spatial dimension. In engineering practice, DG is typically quantified and evaluated via the ECC, and their mathematical relationship is expressed as follows:

$$\mathrm{DG} = 10\sqrt{1 - \mathrm{ECC}^2} \tag{2}$$

Figure 8 illustrates the simulated results of the ECC and DG for the proposed MIMO antenna across the entire operating band. Specifically, Fig. 9(a) demonstrates that within the UWB range of 4.4–26 GHz, the inter-element ECC values exhibit exceptional stability, with peak values consistently maintained below 0.00013. This result not only is far below the universally accepted academic threshold of 0.5 but also outperforms most state-of-the-art UWB MIMO antenna designs. Such negligible correlation provides strong evidence that the improved cross-shaped decoupling structure effectively suppresses surface wave currents, enabling the signals captured by each element to achieve near-perfect statistical independence. Simulta-

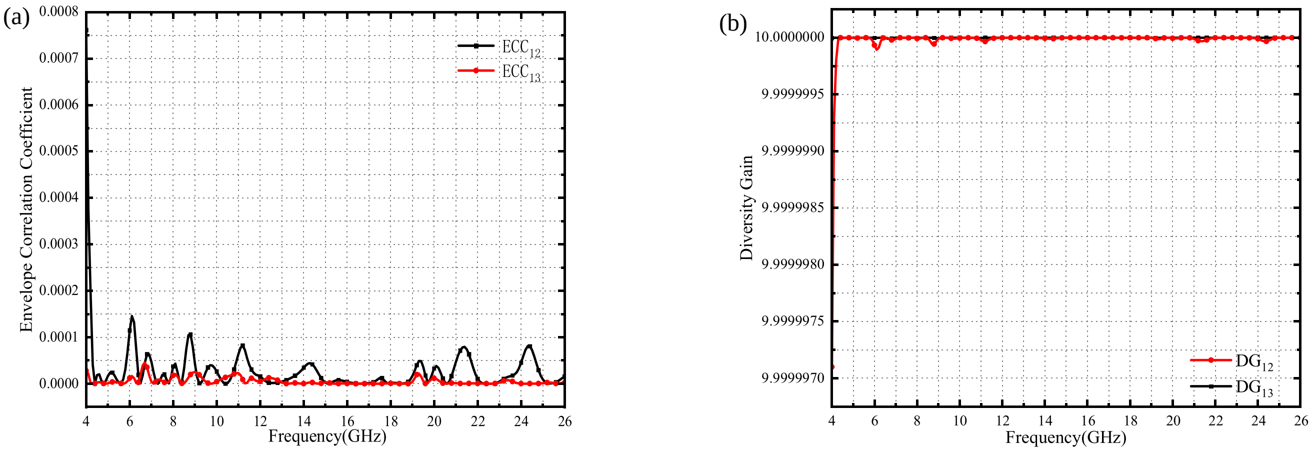

FIGURE 9. (a) ECC, (b) DG.

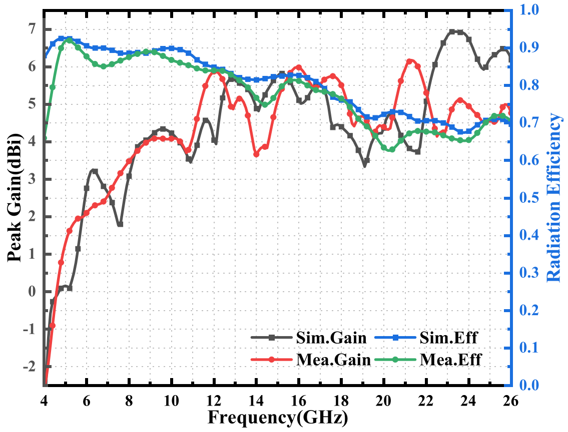

FIGURE 10. Antenna peak gain and radiation efficiency.

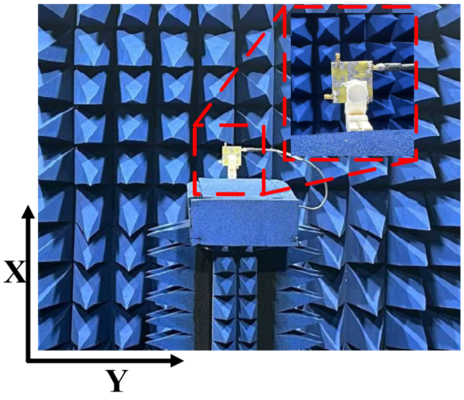

FIGURE 11. Measured in microwave anechoic chamber.

neously, as shown in Fig. 9(b), the DG of the proposed antenna remains stable above 9.9999999 dB throughout the operating bandwidth, with the curve nearly forming a horizontal line that aligns with the ideal limit of 10 dB. This quantitatively confirms the system's ability to achieve superior diversity effects in multipath environments, significantly enhancing the SNR at the receiver while substantially improving the anti-fading capability of the communication link. These findings fully validate the potential of this design for high-performance MIMO communication systems.

3.4. Antenna Peak Gain and Efficiency

Figure 10 presents a comparison between the simulated and measured peak gains and radiation efficiencies of the proposed MIMO antenna. To validate the simulation, the prototype was characterized in a far-field microwave anechoic chamber. The radiation efficiency was obtained using the pattern integration method, where the 3D radiation patterns were measured and integrated over the entire sphere at discrete frequency intervals. As observed, the measured peak gain (red line) tracks the simulated trend (black line) closely, varying from -0.16 dBi to 6.93 dBi. The slight fluctuations and the upward trend at higher frequencies are primarily due to the increased electrical size of the radiators. Regarding radiation performance, the measured efficiency (green line) ranges from 67.4% to 92.6%, showing good agreement with the simulated blue curve. The slight discrepancy (approx. 2–5%) between the simulated and measured results is mainly attributed to the insertion loss of the SMA connectors and cable loss during the testing process. Despite using a cost-effective FR4 substrate, the design maintains superior efficiency across the 4.4–26 GHz band. This confirms that the optimized geometry and refined feeding network effectively mitigate the dielectric losses of FR4, making the antenna highly suitable for high-capacity, low-cost commercial UWB MIMO applications.

3.5. Radiation Performance Analysis of the Antenna

Figure 10 depicts the measurement setup of the fabricated antenna within an anechoic chamber. Fig. 11 presents the comparison between the simulated and measured 2D radiation patterns in the XOZ and YOZ planes at four resonant frequencies: 4.8 GHz, 9.6 GHz, 15.5 GHz, and 22.3 GHz. As shown in Figs. 12(a) and 12(b), the measured patterns exhibit high consistency with the simulated results at lower frequencies. The antenna demonstrates excellent quasi-omnidirectional radiation characteristics in both the XOZ and YOZ planes. This stable radiation distribution ensures wide-angle spatial coverage

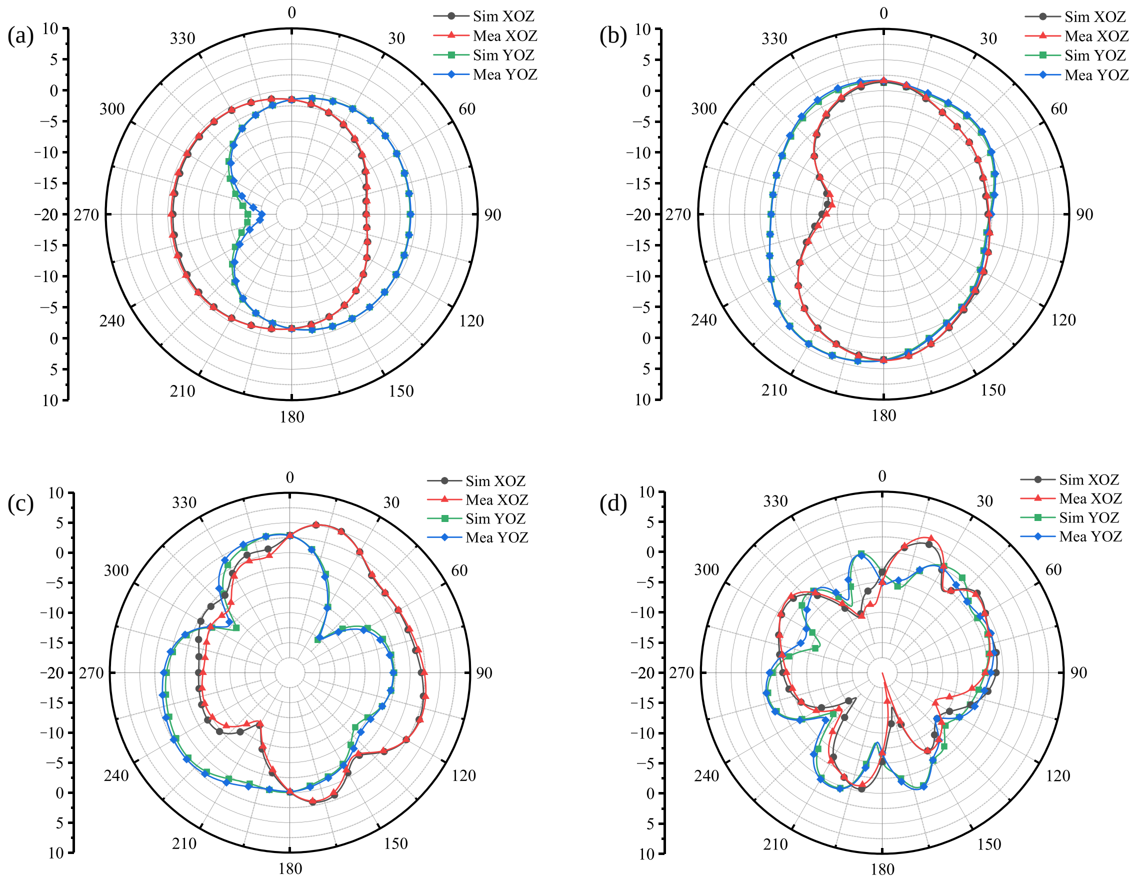

FIGURE 12. 2D radiation patterns. (a) 4.8 GHz, (b) 9.6 GHz, (c) 15.5 GHz, (d) 22.3 GHz.

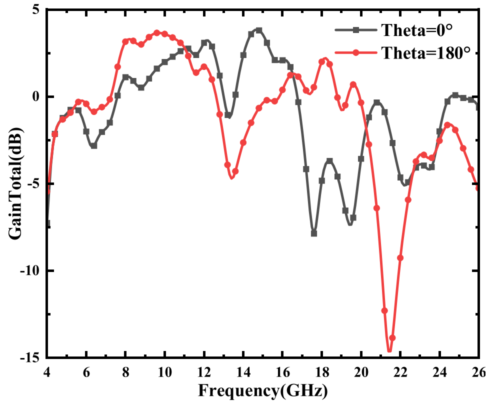

FIGURE 13. Simulated total gain at Theta $= 0°$ and Theta $= 180°$ versus frequency.

TABLE 2. Front-to-back (F/B) ratios at different resonant frequencies.

Frequency (GHz)	Front Gain (dB)	Back Gain (dB)	F/B Ratio
4.8	−1.227	−1.33	0.084 dB
9.6	1.614	3.656	−2.042 dB
15.5	2.287	−0.262	2.549 dB
22.3	-5.070	−6.689	1.619 dB

during low-frequency operation, effectively supporting robust signal reception for UWB systems in complex multipath environments. At 15.5 GHz, as illustrated in Fig. 12(c), the antenna maintains a decentralized radiation state across all observation planes. However, minor fluctuations occur at the pattern boundaries due to the excitation of higher-order resonance modes. This phenomenon is attributed to the reduced wavelength at higher frequencies, which leads to a more complex surface current distribution on the radiating patch and subsequent perturbations in radiation intensity. At the upper frequency bound of 22.3 GHz in Fig. 12(d), the radiation patterns inevitably undergo significant distortions, accompanied by multiple side lobes and nulls. This is primarily because the antenna's physical dimensions are no longer electrically small relative to the operating wavelength. Furthermore, the intensified near-field interactions between the elements result in increased directivity in specific directions. Despite these high-frequency effects, the antenna maintains a broad beamwidth overall without severe energy concentration, thereby preserving robust MIMO diversity performance.

To further evaluate the radiation stability and directional characteristics of the proposed UWB MIMO antenna, the total gains in the forward (Theta $= 0°$) and backward (Theta $= 180°$) directions are compared, as illustrated in Fig. 13. The corresponding front-to-back (F/B) ratios at four key resonant frequencies (4.8, 9.6, 15.5, and 22.3 GHz) are quantitatively summarized in Table 2. The results show that the F/B ratios are 0.084 dB, −2.042 dB, 2.549 dB, and 1.619 dB, respectively. These values remain close to 0 dB across the entire UWB, indi-

TABLE 3. Comparison of the proposed antenna with several existing antennas.

Ref.	Size (mm^2)	BW	No. of Ports	Isolation (dB)	ECC
[13]	54×54	3–14	4	< -22.5	< 0.02
[14]	60×50	2.98–10	2	< -31.4	\
[15]	20×40	5.51–15	2	< -25	\
[16]	92×92	2–14	4	< -15	\
[17]	55×55	4.66–15.97	4	< -20	< 0.035
[18]	30×30	2.2–20	4	< -20	< 0.01
[19]	27×22	3.07–11.1	2	< -20	< 0.014
[20]	55×55	2–16.49	2	< -16	< 0.24
This	47×47	4.4–26	4	< -28	< 0.00013

cating that the antenna maintains a stable quasi-omnidirectional radiation characteristic with a balanced energy distribution in both the forward and backward hemispheres. Such performance is critical for UWB applications, as it ensures reliable signal coverage in complex multipath environments.

3.6. Group Delay

To verify the phase linearity and pulse integrity of the proposed UWB MIMO antenna, the group delay is investigated using two identical key-shaped elements in both face-to-face and side-by-side configurations with a separation distance of 200 mm, as shown in Fig. 14. The simulated results indicate that the group delay remains remarkably stable around 0.75 ns and 1.0 ns for the two cases, respectively, which is consistent with the physical propagation time. Across the major portion of the 4.4–26 GHz band, the group delay variation is maintained within 0.15 ns, excluding a few narrow-band spikes caused by transmission zeros. This flat group delay response confirms that the antenna possesses excellent phase linearity and will not cause significant signal dispersion, making it highly suitable for high-speed UWB impulse radio applications.

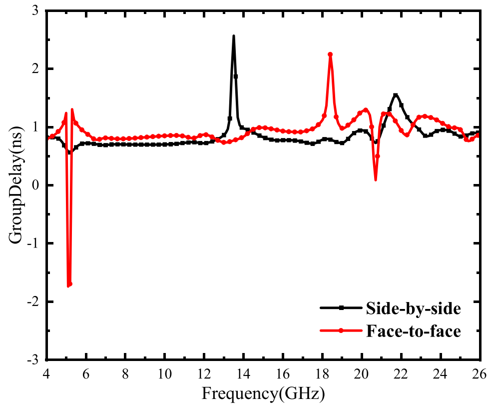

FIGURE 14. Group delay.

3.7. Total Active Reflection Coefficient and Channel Capacity Loss

For MIMO antenna systems, S-parameters alone cannot fully characterize practical performance. Therefore, it is essential to evaluate the Total Active Reflection Coefficient (TARC) of the antenna. TARC can be derived from the S-parameters using the following formula:

$$\text{TARC} = \frac{\sqrt{\sum_{i=1}^{4}\left|S_{i1}+\sum_{n=2}^{4}S_{in}e^{j\theta n-1}\right|}^{2}}{2} \tag{3}$$

Channel capacity loss (CCL) is also a critical performance metric for MIMO antennas. In general, a CCL value lower than 0.4 bps/Hz satisfies the design specifications for MIMO antenna systems. The channel capacity loss can be expressed as follows:

$$\text{CCL} = -\log_2 \det\left|\psi^R\right| \tag{4}$$

$$\psi^R = \begin{pmatrix} \rho_{11} & \cdots & \rho_{1n} \\ \vdots & \ddots & \vdots \\ \rho_{m1} & \cdots & \rho_{mn} \end{pmatrix} \tag{5}$$

As shown in Fig. 15(a), the TARC was calculated for several sets of characteristic phases. It can be observed that the TARC remains below -10 dB (mostly below -15 dB) across the entire operating bandwidth of 4.4–26 GHz. Notably, the TARC curves corresponding to different phase combinations almost completely overlap. This phenomenon is mainly attributed to the high isolation and structural symmetry of the proposed four-port MIMO antenna. The results demonstrate that the antenna exhibits highly stable impedance bandwidth independent of the incident signal phase, ensuring reliable operating performance in practical multipath environments.

Figure 15(b) illustrates the CCL of the antenna. A slight fluctuation in CCL is observed near 6.96 GHz, with a peak value of approximately 0.5 bps/Hz. This is mainly attributed to the high sensitivity of the four-port correlation matrix to return loss. Nevertheless, over the entire UWB bandwidth of 4.4–26 GHz, the CCL remains below 0.3 bps/Hz in most frequency bands, and the return loss S_{11} is less than 10 dB. Therefore, this minor deviation does not degrade the overall high-speed communication performance of the system.

A comprehensive comparison between the proposed antenna and several state-of-the-art designs reported in recent years is

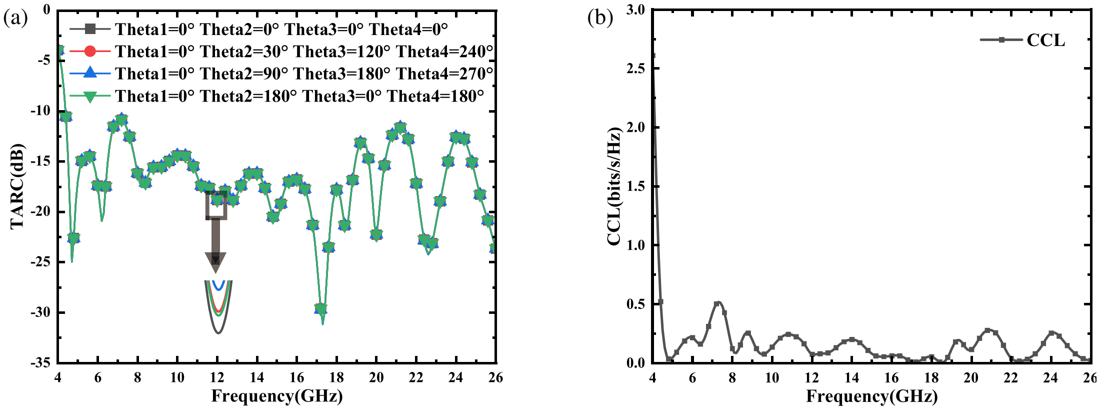

FIGURE 15. (a) TARC; (b) CCL.

summarized in Table 3. The results demonstrate that the proposed design exhibits significant competitive advantages across multiple key performance metrics. Regarding bandwidth performance, the antenna achieves an UWB coverage from 4.4 to 26 GHz, which significantly outperforms existing works and demonstrates superior spectrum utilization and extension capabilities. In terms of core MIMO parameters, the proposed design maintains a multi-port configuration while delivering excellent decoupling characteristics, with port isolation better than -28 dB and an ECC as low as the 10-4 level. Such low ECC values indicate exceptional radiation decorrelation between channels, which effectively enhances the system channel capacity. Furthermore, considering the trade-off between size and performance, the proposed antenna features a highly competitive compact structure compared to other multi-port wideband designs, maintaining optimal electromagnetic performance while minimizing the physical footprint. Overall, the proposed antenna achieves an ideal balance among ultra-wideband operation, high isolation, and miniaturization, highlighting its substantial potential for practical engineering applications.

4. CONCLUSION

A compact four-port UWB-MIMO antenna featuring both miniaturization and high isolation has been successfully designed, fabricated, and validated. By leveraging the geometric evolution of key-shaped radiators and a strategically placed cross-shaped decoupling structure, the proposed design effectively overcomes the challenge of achieving high isolation in shared-ground systems across an ultra-wide frequency range. The results indicate that the antenna provides stable operation from 4.4 to 26 GHz. Notably, the isolation $>$ 28 dB and ECC $<$ 0.00013 metrics significantly outperform existing state-of-the-art designs. The high degree of consistency between simulations and measurements further confirms the robustness of the proposed scheme. In summary, the antenna achieves an optimal balance between miniaturization, wideband characteristics, and decoupling performance, demonstrating its substantial potential for future high-capacity and high-speed wireless applications.

ACKNOWLEDGEMENT

This work was supported in part the International Joint Research Center for Intelligent Sensing and High-Dimensional Modeling of Ancient Buildings in Anhui Province under No. GJZZX2025KF01.

REFERENCES

[1] Zheng, X., Y. Zhang, and L. Yue, "High isolation UWB MIMO notch antenna based on metamaterials," *Progress In Electromagnetics Research C*, Vol. 169, 55–65, 2026.

[2] Jayant, S., G. Srivastava, and S. Kumar, "Quad-port UWB MIMO footwear antenna for wearable applications," *IEEE Transactions on Antennas and Propagation*, Vol. 70, No. 9, 7905–7913, Sep. 2022.

[3] Shailesh, G. Srivastava, S. Kumar, et al., "Compact UWB MIMO antenna with a modified back reflector and supported by characteristic mode analysis for wireless communication applications," *IEEE Access*, Vol. 12, 187 302–187 312, 2024.

[4] Tu, R., H. Lin, and Z. Wang, "A MIMO ultra-wideband antenna with high isolation and triple notches," *Progress In Electromagnetics Research C*, Vol. 159, 91–102, 2025.

[5] Hussain, R., M. S. Sharawi, and A. Shamim, "An integrated four-element slot-based MIMO and a UWB sensing antenna system for CR platforms," *IEEE Transactions on Antennas and Propagation*, Vol. 66, No. 2, 978–983, Feb. 2018.

[6] Nie, L. Y., X. Q. Lin, Z. Q. Yang, J. Zhang, and B. Wang, "Structure-shared planar UWB MIMO antenna with high isolation for mobile platform," *IEEE Transactions on Antennas and Propagation*, Vol. 67, No. 4, 2735–2738, Apr. 2019.

[7] Gómez-Villanueva, R. and H. Jardón-Aguilar, "Compact UWB uniplanar four-port MIMO antenna array with rejecting band," *IEEE Antennas and Wireless Propagation Letters*, Vol. 18, No. 12, 2543–2547, Dec. 2019.

[8] Zhao, X., S. P. Yeo, and L. C. Ong, "Planar UWB MIMO antenna with pattern diversity and isolation improvement for mobile platform based on the theory of characteristic modes," *IEEE Transactions on Antennas and Propagation*, Vol. 66, No. 1, 420–425, Jan. 2018.

[9] Peitzmeier, N., T. Hahn, and D. Manteuffel, "Systematic design of multimode antennas for MIMO applications by leveraging symmetry," *IEEE Transactions on Antennas and Propagation*, Vol. 70, No. 1, 145–155, Jan. 2022.

[10] Nejdi, I. H., M. Marzouk, M. A. Lafkih, S. Bri, J. A. Nasir, Z. Zakaria, and A. J. A. Al-Gburi, "A low-profile UWB monopole antenna and high-isolated UWB-MIMO antenna for wireless communications networks," *Progress In Electromagnetics Research C*, Vol. 161, 105–119, 2025.

[11] Khedr, A. A., B. E. Elnaghi, and A. M. Mohamed, "Design of a compact dual port 2×1 ultra-wideband MIMO antenna for radio frequency energy harvesting based on four "a" shaped slots," *Progress In Electromagnetics Research M*, Vol. 128, 41–49, 2024.

[12] Wang, Z., G. Song, W. Nie, M. Yang, C. Li, and M. Wang, "A racket-like UWB MIMO antenna with high isolation," *Progress In Electromagnetics Research C*, Vol. 144, 159–168, 2024.

[13] Nagavardhani, K., P. R. Kumar, and V. M. Rao, "A miniaturized highly isolated quad-port penta-band-notched UWB MIMO antenna based on EBG structures," *Progress In Electromagnetics Research C*, Vol. 166, 19–26, 2026.

[14] Nie, L. Y., X. Q. Lin, S. Xiang, B. Wang, L. Xiao, and J. Y. Ye, "High-isolation two-port UWB antenna based on shared structure," *IEEE Transactions on Antennas and Propagation*, Vol. 68, No. 12, 8186–8191, Dec. 2020.

[15] Liu, S., J. Nan, and Y. Wang, "Improvement of isolation and bandwidth of notch ultra-wideband MIMO antenna on metamaterial wall," *Progress In Electromagnetics Research C*, Vol. 163, 43–49, 2026.

[16] Jayant, S. and G. Srivastava, "Close-packed quad-element triple-band-notched UWB MIMO antenna with upgrading capability," *IEEE Transactions on Antennas and Propagation*, Vol. 71, No. 1, 353–360, Jan. 2023.

[17] Zheng, X., L. Yue, and Y. Zhang, "A compact four-port axially symmetric UWB-MIMO antenna array: Metamaterial-integrated coplanar waveguide for broadband operation with high isolation," *Progress In Electromagnetics Research C*, Vol. 162, 58–69, 2025.

[18] Firdaus, F., R. Kurnia, and I. Elfitri, "Compact UWB MIMO antenna with minangkabau roof-inspired patch and L-shaped ground strip for enhanced bandwidth," *Progress In Electromagnetics Research C*, Vol. 161, 178–187, 2025.

[19] Li, W., L. Wu, S. Li, X. Cao, and B. Yang, "Bandwidth enhancement and isolation improvement in compact UWB-MIMO antenna assisted by characteristic mode analysis," *IEEE Access*, Vol. 12, 17 152–17 163, 2024.

[20] Srivastava, G., S. Kumar, O. P. Kumar, *et al.*, "Triple-band notched and highly decoupled MIMO antenna using characteristic mode analysis," *IEEE Access*, Vol. 13, 165 956–165 969, 2025.